www.MaterialsViews.com

ADVANCED MATERIALS

www.advmat.de

COMMUNICATION

Graded Doping for Enhanced Colloidal Quantum Dot Photovoltaics

*Zhijun Ning, David Zhitomirsky, Valerio Adinolfi, Brandon Sutherland, Jixian Xu, Oleksandr Voznyy, Pouya Maraghechi, Xinzheng Lan, Sjoerd Hoogland, Yuan Ren, and Edward H. Sargent**

Colloidal quantum dot (CQD) based optoelectronic devices have attracted great interest in recent years due to their facile solution-processing and quantum-size-effect-enabled bandgap tunability.[1–7] This makes them ideal materials for the active absorbing layer in solar cells, where large-area processing is required, and where multiple junction approaches and multiple exciton generation offer the potential to raise performance beyond the single-junction Shockley–Quiesser limit.[3,5,8]

Rapid advances in CQD solar cell device architecture and materials electronic properties have led to record AM1.5 solar power conversion efficiencies of 7%.[9] To gain control over the electronic properties of these materials, as well as to enable the realization of families of more functionally complex devices such as bipolar transistors and thyristors, much work has been devoted to incorporating specific dopants that will control the free carrier density in quantum solid films.[10–14] Recently, PbS CQDs have been tailored to be either p-type and n-type,[15,16] allowing for the fabrication of high-efficiency, all-inorganic, all-CQD p-n junction solar cells.[17,18]

In spite of rapid recent progress, the efficiencies achieved to date leave much room for further improvement. One remaining challenge in the electronic materials properties of CQD solids is the relatively short minority carrier diffusion length, which is typically on the order of, or in cases considerably less than, 100 nm.[19] Increasing film thickness with the goal of increasing absorbance does not result in increased efficiencies when the un-depleted device thickness exceeds this diffusion length.[20] Depleted bulk heterojunction structures have been introduced,[21,22] where the electrode material and CQD layers interpenetrate to maximize absorbance without sacrificing charge collection. Furthermore, the quantum funnel – a conduction band-edge grading scheme that leveraged CQD bandgap tunability – enhanced carrier collection by extending the depth of film in which a significant electrical field provided for drift-based electron extraction.[23] Improving CQD surface passivation has been used to reduce trap density[24,25] in CQD solids,[9] also enhancing film and device performance.

In the present manuscript, we explore a newly enhanced degree of freedom in engineering the electronic properties in CQD solids – control over doping[15] – and prove that it can be exploited to improve device performance. A p-n junction device, termed quantum junction (QJ),[17] was recently reported based on control over quantum dot solid net doping type and amplitude, and offering the benefit of quantum-size-effect tuning of each side of the junction.

Our strategy in the present work is depicted in **Figure 1**a and b. The previously reported quantum junction device, seen in Figure 1a, relies on rather low doping (≈10^{16} cm^{-3}) of the thick n-layer active region. This low doping is accompanied by low trap state densities and thus is beneficial for both transport and recombination. However, the low doping also reduces the built-in potential, a determinant of the open-circuit voltage; and entails a tapering off in the amplitude of the electric field near the back side of the device – the region in which drift-driven transport is most urgently needed to extract the photocharges generated most remotely from the charge-separating front p-n junction. Using a more heavily-doped n-region can increase the open circuit voltage but at the expense of having a reduced depletion region. Such a compromise would curtail carrier extraction, leading to a significantly reduced photocurrent.

In Figure 1b, we propose a device architecture in which we replace the top 30 nm of lightly doped n-type solid with a highly doped (10^{17}–10^{18} cm^{-3}) n^+ CQD layer, keeping the total thickness and thus absorbance fixed.[17,18] Figure 1c,d depict spatial band diagrams at the maximum power-point of these two devices, simulated using SCAPS 3.0.01[26,27] and previously established methods,[17,24,28] and employing the material parameters listed in the methods section, assuming AM1.5G solar illumination.

The benefit of introducing the highly-doped n^+ layer is two-fold. It introduces an electric field in the rear of the device to aid in carrier extraction, resulting in increased current at the maximum power point. As well, it allows for greater electron and hole quasi-Fermi level splitting at the maximum power point, resulting in an increased operating voltage.[29]

We explored device behavior at the maximum power point (Figures 1e,f) and found that both the operating voltage and currents (V_{MPP} and J_{MPP}) increase with increasing doping in the heavier doped n^+ region (10^{15} cm^{-3} n-layer, and 10^{15}–10^{19} cm^{-3} n^+ doping variation). Grading the doping profile in such a way could contribute to a 1.3× increase in the power conversion

Dr. Z. Ning,[+] D. Zhitomirsky,[+] V. Adinolfi, B. Sutherland, J. Xu, Dr. O. Voznyy, P. Maraghechi, X. Lan, Dr. S. Hoogland, Dr. Y. Ren, Prof. E. H. Sargent
Department of Electrical and Computer Engineering
University of Toronto, 10 King's College Road
Toronto, Ontario, M5S 3G4, Canada
E-mail: ted.sargent@utoronto.ca

[+]Z. Ning and D. Zhitomirsky contributed equally to this work.

DOI: 10.1002/adma.201204502

© 2013 WILEY-VCH Verlag GmbH & Co. KGaA, Weinheim

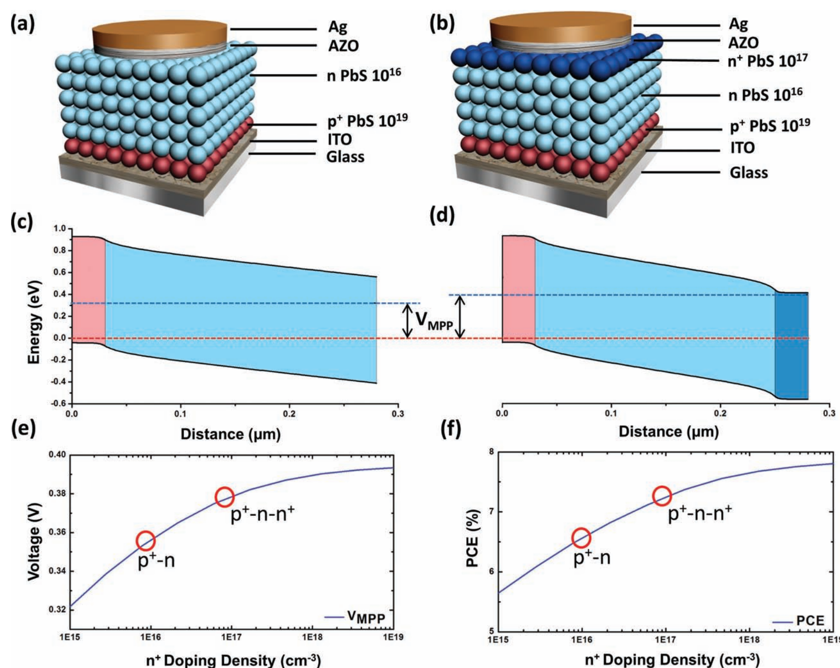

Figure 1. a,b) Ungraded (a) and graded (b) CQD solar cells. c,d) Simulated spatial band diagrams of the ungraded (c) and graded (d) devices operating at the maximum power point. The graded device shows a >20% increase in operating voltage (V_{MPP}), and band-bending near the rear of the device introduces an additional electric field capable of aiding with carrier collection for improved fill factor. e,f) Simulated enhancement from the graded doping architecture: the simulations show that as the doping density in the graded scheme is increased, the operating voltage (V_{MPP}) at the maximal power-point is increased. This results in a PCE enhancement with increasing n^+ layer doping.

efficiency (PCE) if very high doping could be achieved without compromise to transport and recombination properties.

We therefore set out to identify experimental means to influence doping of n-type CQD films in a manner that substantially preserved their properties as active materials in photovoltaics. We built upon recent advances in the creation of halides-passivated n-type all-inorganic CQD films.[25]

Using field-effect transistor (FET) studies, we characterized the doping type and transport behavior in a variety of films.[15,30] The transistor consisted of an aluminum gate, aluminum-oxide/octadecyltrichlorosilane hybrid gate dielectric, PbS CQD film and titanium source and drain electrodes. The FET transfer characteristics (**Figure 2**a) show that a positive gate voltage generates a current between source and drain, characteristic of an n-type film. The equation for the doping density calculation is shown in the Supporting Information S1. Using a short bromide soak vs. a long iodide soak during film fabrication led to a greater conductivity for the iodine treated film (Figure 2b) and allowed us to form either lightly 10^{16} cm^{-3} or heavily 10^{17} cm^{-3} doped layers, respectively (Figure 2c). The error bars for the doping density values are shown in Figure 2c. The particular choice of halogen and soaking time was optimal for making a suitable lightly or heavily doped layer in each case based on the respective halogen reactivity with this class of PbS CQDs. The electron mobility in each film was similar at 0.01 cm^2/Vs (Figure 2d). The approach leveraged the high degree of accessibility to the surface of the CQD semiconductor nanoparticles afforded by a high surface area to volume ratio of our ≈3 nm particles. This increases the likelihood of replacing sulfur atoms with halogen dopants required to implement n-doping the CQD film. XPS confirmed the greater presence of halide ions in the iodide treated films compared with the bromide treated films (Figure 2e). Soaking with the iodide for different durations was also previously shown to result in differing doping densities,[15] and had also resulted in different trap density profiles;[25] hence, though 10^{18} cm^{-3} doping is possible with the halide ion approach, the films are not, in their present form, photovoltaic-device-grade materials.

We constructed two classes of devices employing these materials to elucidate the benefit of graded doping. The device architectures are akin to those presented in Figures 1a and 1b, where bromide-treated films are used as the lightly-doped n-type active layers in each case; and, in the graded-doping device, an iodide-treated replaces the final layer with a heavily-doped n^+-layer.

We sought a means of confirming that the doping gradient – ascertained from FET measurements – was manifested in the electronic properties of the final device. We expected that a graded doping profile should change the capacitance vs. voltage behavior of the device.[31]

We begin by depicting Mott–Schottky analysis of the conventional, ungraded, asymmetric p-n junction device. For bias levels more negative than required to achieve full depletion of the lightly-doped n-layer, the capacitance is essentially constant, since bias cannot further deplete the device. For voltages more positive than this threshold bias, capacitance grows as the depletion narrows, its boundary progressing inwards. The slope of the $1/C^2$ vs. V curve allows the doping of the lesser-doped side of the asymmetric junction to be inferred (Supporting information S2).

As **Figure 3**a illustrates, analogous logic allows the doping levels in each of the two n-type regions of the p-n-n^+ device to be extracted. At the most strongly negative biases, the entire n-doped side of the device is fully depleted, and the capacitance is substantially constant. As the applied voltage is increased in the positive direction, a quasi-neutral region develops in the more heavily-doped n^+ region, and the slope of $1/C^2$ vs V reveals the n^+ side's doping. Only once the n^+ region has been returned to complete quasi-neutrality, and the depleted-to-quasi-neutral boundary layer begins to penetrate into the lightly-doped n-region, does $1/C^2$ begin to describe the doping in the n-layer.

Graded and ungraded devices were each constructed to have a total n-type material thickness of 250 nm. In the graded case, the final 30 nm of the device consisted of the heavily doped n^+ layer. Since using a large n^+ layer thickness can significantly reduce the depleted portion of this region and thus result in carrier loss (Supporting Information S3), we instead employed a thin n^+ layer. Figure 3b shows the experimental $1/C^2$ curves

© 2013 WILEY-VCH Verlag GmbH & Co. KGaA, Weinheim

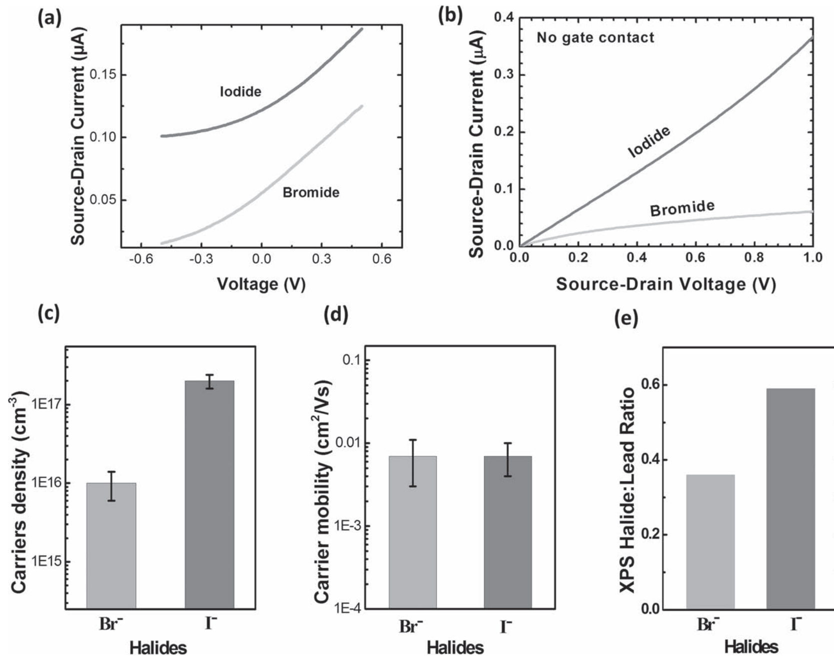

Figure 2. a) Experimental FET transfer curves showing n-type modulation for channels formed using halide-treated materials. b) FET response without a gate bias, showing a marked difference in conductivity between these two films. The difference in conductivity is attributed to differences in free carrier density since FET analysis reveals comparable linear mobilities. c,d) Extracted doping densities and carrier mobilities for the two types of FETs. e) XPS analysis showing that iodine leads to highest halogen content compared with bromine solid state treatments.

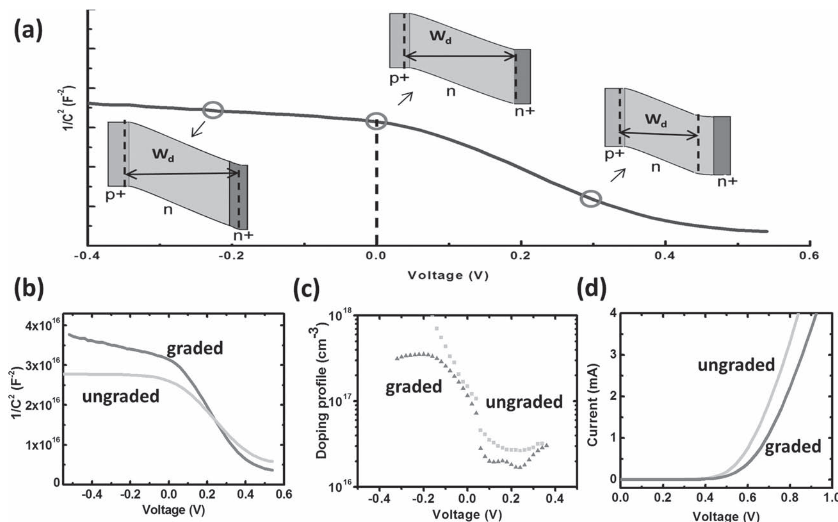

Figure 3. a) The regimes of depletion in a graded device. b) Experimental capacitance–voltage response of the graded and ungraded structures. The ungraded architecture has a single well defined slope in the Mott–Schottky analysis, corresponding to a single doping density. In contrast, the graded structure exhibits two distinct slopes consistent with two differently doped layers. c) Extracted doping densities based on the Mott–Schottky analysis at each voltage point. d) Dark *I–V* curves of the graded and ungraded devices highlighting the differences in built in voltage.

obtained for each device, and, using Mott–Schottky analysis (Figure 3c), we were able to extract doping densities for each case by calculating the slope at each point in the various regions discussed in Figure 3a. Analysis of the ungraded device resulted in a single doping density of 2.5×10^{16} ($\pm 1 \times 10^{16}$) cm^{-3}. This is directly evident from the flat plateau portion of Figure 3c. However, as the device becomes increasingly reversed biased, the apparent doping density grows dramatically because the device has attained full depletion and the change in capacitance is marginal – hence there is only one doped region present. In contrast, the graded device exhibits two plateaus indicative of two different doping densities, and the analysis results in an n region doping density of 2×10^{16} ($\pm 1 \times 10^{16}$) cm^{-3} and an n$^+$ region doping density of 2×10^{17} ($\pm 1 \times 10^{17}$) cm^{-3}. The extracted doping density change trend agrees well with the extracted FET doping densities taking into account the experimental error and variation associated with both of these measurements. Furthermore, the doping densities extracted from both Cap–*V* curves agree within error for both the lightly doped material. The graded devices are not fully depleted at 0 V, while the ungraded devices are fully depleted – consistent with the addition of the n$^+$ region sufficiently heavily doped to retain a quasi-neutral region at the edge of the device.

The dark *I–V* characteristics (Figure 3d) of the solar cells to illustrate that the diode turn-on voltage, which depends on the built-in voltage, is greater for the graded structure – boding well for such a device achieving a higher operating voltage under solar illumination.

Current–voltage measurements of the same devices were obtained under AM1.5 solar power illumination (**Figure** 4a). The open circuit voltage (V_{oc}) is greater for the graded case (0.55 V vs. 0.51 V), attributed the greater built-in potential afforded by the n$^+$ layer. The fill factor of the device had increased as well (55% vs. 52%), attributable to the enhancement due the introduced electric field at the n/n$^+$ interface. The short circuit current density (J_{SC}) had not increased substantially, consistent with the fact that the ungraded device was already at full depletion when unbiased (Figure 3). The external quantum efficiency (EQE) spectra of both devices were shown in the Supporting Information S4). The graded device show a bit increased EQE in the infrared region. The champion efficiency of the graded device was 7.4% compared to the 6.4% achieved with

© 2013 WILEY-VCH Verlag GmbH & Co. KGaA, Weinheim

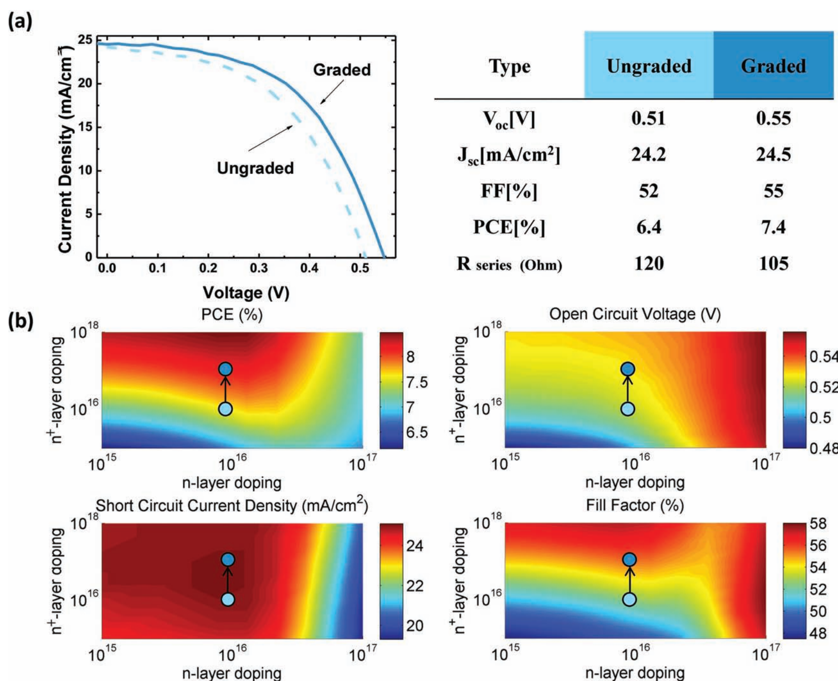

Type	Ungraded	Graded
V_{oc}[V]	0.51	0.55
J_{sc}[mA/cm^2]	24.2	24.5
FF[%]	52	55
PCE[%]	6.4	7.4
R series (Ohm)	120	105

Figure 4. a) Experimental I–V curves and champion performance of the devices under AM 1.5 illumination. The graded device shows higher V_{oc} and FF than the ungraded one. The overall PCE value of the graded device is 1% higher, leading to a record performance of all-inorganic CQD solar cells. b) Simulated solar cell parameters as a function of n-layer doping and n$^+$-layer doping. These self-consistent simulations show that the PCE may be increased by increasing the n$^+$ region doping, with enhancements to both fill factors and open circuit voltage. Simulated device data points for the ungraded and graded devices have been included as a guide to the eye for the reader, showing the expected changes in critical device parameters for ease of comparison with actual device data.

the ungraded device, a record efficiency for all-inorganic CQD devices.

We conclude with an exploration (Figure 4b) of the quantitative extent of performance benefits achievable with further optimization of the graded doping strategy. The open circuit voltage benefits from increased doping in each layer, particularly in the n$^+$-layer, and stands to improve 10%. The fill factor (FF) stands to benefit to a similar degree from an increase in the n$^+$-layer doping. Increasing the n$^+$-layer to 10^{18} cm^{-3}, if it can be done without significant compromise to other electronic materials parameters, offers an avenue to over 8% PCE. Further increases in the doping density may be achieved by using the recently reported redox couples[30] or tuning the stoichiometry of the underlying nanocrystal material composition.[16]

We have constructed a new kind of graded-doping, all-inorganic, all-CQD solar cell. The constituent CQD layers are tailored to have different doping densities via the use of controllable halide treatment strategy. The graded scheme allows for greater operating and open circuit voltages due to enhanced built-in voltage, while the added electric field enhances carrier collection at the maximum power-point. A similar grading scheme could potentially be implemented in the depleted heterojunction architectures once fine control over doping density and material compatibility is achieved in p-type PbS materials. For the quantum junction architecture, the graded doping scheme reported herein resulted in a 1 power point PCE improvement for this class of devices, and stands to increase to over 8% PCE once the doping density in the n$^+$-layer produces device-grade materials with a doping density of 10^{18} cm^{-3} or greater.

Experimental Section

CQD Synthesis and Solution Halide Treatment: PbS CQDs were synthesized according to a published recipe.[21] Solution pre-treatment was carried out with tetrabutylammonium iodide (TBAI).[25]

Film Deposition: The p-type film was prepared using a dip-coating process. ITO-coated glass was dipped into a CQD solution (8 mg/mL) in hexane for 20 s, and then dried in air for 300 seconds. The film was then dipped into a tetramethylammonium hydroxide methanol solution (10 mg/mL) for 25 s, and then dried at room temperature for 2 minutes. Finally, the film was dipped into methanol for 3 seconds, and dried for 200 seconds. This cycle was repeated three times to reach a final thickness of 30 nm.

The n-type film fabrication process is similar to previous reports.[17] For the intermediate n-type layer, tetrabutylammonium bromide (30 mM) was used for the ligand exchange with a soak time of 10 seconds and with a final 220 nm thickness was achieved. For the n$^+$ layer, a TBAI in methanol (30 mM) solution was used with a treatment time of 60 seconds, to reach a final thickness of 30 nm.

FET Measurement: Thermal deposition of Al was carried out on glass, and the surface of Al layer was then electrochemically anodized to form an 8 nm thick Al_2O_3 gate dielectric. This was followed by spin coating of PbS CQDs in a N_2 glovebox, and treatment with 30 mM TBAI (2 × 60 s) or TBAB (2 × 10 s) in methanol, to form 50 nm thick films. Finally, titanium was deposited for the top source and drain contacts. The FETs had a channel width of 2 mm, and channel length of 50 µm Carrier mobility was extracted from the linear portion of the I–V curve.

PCE Characterization: Current–voltage characteristics were measured using a Keithley 2400 source-meter in N_2 ambient. The solar spectrum at AM1.5 was simulated to within class A specifications (less than 25% spectral mismatch) with a Xe lamp and filters (Solar Light Company Inc.) with measured intensity at 100.6 mW cm^{-2}. The source intensity was measured using a Melles-Griot broadband power meter and a Thorlabs broadband power meter through a circular 0.05 cm^2 aperture at the position of the device and confirmed with a calibrated reference solar cell (Newport, Inc.). The accuracy of the power measurement was estimated to be ±5%.

Cap–V Measurement: Capacitance–voltage (C–V) measurements were performed using an Agilent 4284A precision LCR meter under Cp-Rp model. All measurements were performed in the dark. CV sweeps of solar cell devices were performed between −1 V and 1 V with an AC signal of 10 mV and 1000 Hz.

Optoelectronic Simulation: SCAPS 3.0.01 was used for the optoelectronic simulations. The p-n junction devices were simulated with a p-layer thickness of 30 nm, and a doping of ≈10^{19} cm^{-3}. The p-layer mobility was 10^{-3} cm^2/Vs, with a trap density of 10^{16} cm^{-3} 0.3 eV below the conduction band. The n-layer thicknesses were modeled according to those reported in the manuscript. All n-layers included trap densities of 10^{15} cm^{-3}, 0.2 eV above the valence band. Mobilities of 10^{-2} cm^2/Vs were used. Doping densities were varied from 10^{15} to 10^{19} cm^{-3} depending on the simulation. A band-gap of 1 eV was used for the CQDs to account for the difference between the optical and electronic bandgaps. The

© 2013 WILEY-VCH Verlag GmbH & Co. KGaA, Weinheim

boundary conditions at each end were ohmic. An AM1.5 G illumination spectrum was used for the device excitation.

Supporting Information

Supporting Information is available from the Wiley Online Library or from the author.

Acknowledgements

This publication is based in part on work supported by Award KUS-11-009-21, made by King Abdullah University of Science and Technology (KAUST), by the Ontario Research Fund Research Excellence Program, and by the Natural Sciences and Engineering Research Council (NSERC) of Canada. D.Z. acknowledges support from the NSERC CGS D scholarship. We thank Angstrom Engineering, Inc. and Innovative Technology, Inc. for useful discussions regarding material deposition methods and control of the glovebox environment, respectively. The authors thank: Larissa Levina for the assistance of quantum dots synthesis, Xihua Wang, Susanna Thon for helpful discussion; André Labelle and Daniel Paz-Soldan for measurement asisstance; and E. Palmiano, R. Wolowiec, and D. Kopilovic for their help during the course of study.

Received: October 31, 2012
Revised: December 8, 2012
Published online: February 5, 2013

[1] M. Grätzel, R. A. J. Janssen, D. B. Mitzi, E. H. Sargent, *Nature* **2012**, *488*, 304–312.
[2] L. Etgar, W. Zhang, S. Gabriel, S. G. Hickey, M. K. Nazeeruddin, A. Eychmüller, B. Liu, M. Grätzel, *Adv. Mater.* **2012**, *24*, 2202–2206.
[3] X. Wang, G. I. Koleilat, J. Tang, H. Liu, I. J. Kramer, R. Debnath, L. Brzozowski, D. A. R. Barkhouse, L. Levina, S. Hoogland, E. H. Sargent, *Nat Photonics* **2011**, *5*, 480–484.
[4] A. K. Rath, M. Bernechea, L. Martinez, F. P. G. de Arquer, J. Osmond, G. Konstantatos, *Nat Photonics* **2012**, *6*, 529–534.
[5] A. Nozik, M. Beard, J. Luther, M. Law, R. Ellingson, J. Johnson, *Chem. Rev.* **2010**, *110*, 6873.
[6] D. V. Talapin, J. S. Lee, M. V. Kovalenko, E. V. Shevchenko, *Chem. Rev.* **2010**, *110*, 389.
[7] Z. Ning, H. Tian, H. Qin, Q. Zhang, H. Ågren, L. Sun, Y. Fu, *J. Phys. Chem. C* **2010**, *114*, 15184–15189.
[8] C. H. Henry, *J. Appl. Phys.* **1980**, *51*, 4494–4500.
[9] A. H. Ip, S. M. Thon, S. Hoogland, O. Voznyy, D. Zhitomirsky, R. Debnath, L. Levina, L. R. Rollny, G. H. Carey, A. Fischer, K. W. Kemp, I. J. Kramer, Z. Ning, A. J. Labelle, K. W. Chou, A. Amassian, E. H. Sargent, *Nat. Nanotechnol.* **2012**, *7*, 577–582.
[10] D. V. Talapin, C. B. Murray, *Science* **2005**, *310*, 86–89.
[11] H. Liu, S. Keuleyan, P. Guyot-Sionnest, *J. Phys. Chem. C* **2011**, *116*, 1344–1349.
[12] A. Sahu, M. S. Kang, A. Kompch, C. Notthoff, A. W. Wills, D. Deng, M. Winterer, C. D. Frisbie, D. J. Norris, *Nano Lett.* **2012**, *12*, 2587–2594.
[13] S. M. Geyer, P. M. Allen, L.-Y. Chang, C. R. Wong, T. P. Osedach, N. Zhao, V. Bulovic, M. G. Bawendi, *ACS Nano* **2010**, *4*, 7373–7378.
[14] D. J. Norris, A. L. Efros, S. C. Erwin, *Science* **2008**, *319*, 1776–1779.
[15] D. Zhitomirsky, M. Furukawa, J. Tang, P. Stadler, S. Hoogland, O. Voznyy, H. Liu, E. H. Sargent, *Adv. Mater.* **2012**, *24*, 6181–6185.
[16] O. Voznyy, D. Zhitomirsky, P. Stadler, Z. Ning, S. Hoogland, E. H. Sargent, *ACS Nano* **2012**, *6*, 8448–8455.
[17] J. Tang, H. Liu, D. Zhitomirsky, S. Hoogland, X. Wang, M. Furukawa, L. Levina, E. H. Sargent, *Nano Lett.* **2012**, *12*, 4889–4894.
[18] H. Liu, D. Zhitomirsky, S. Hoogland, J. Tang, I. J. Kramer, Z. Ning, E. H. Sargent, *Appl. Phys. Lett.* **2012**, *101*, 151112.
[19] J. M. Luther, M. Law, M. C. Beard, Q. Song, M. O. Reese, R. J. Ellingson, A. J. Nozik, *Nano Lett.* **2008**, *8*, 3488–3492.
[20] A. G. Pattantyus-Abraham, I. J. Kramer, A. R. Barkhouse, X. Wang, G. Konstantatos, R. Debnath, L. Levina, I. Raabe, M. K. Nazeeruddin, M. Gratzel, E. H. Sargent, *ACS Nano* **2010**, *4*, 3374–3380.
[21] D. A. R. Barkhouse, R. Debnath, I. J. Kramer, D. Zhitomirsky, A. G. Pattantyus-Abraham, L. Levina, L. Etgar, M. Grätzel, E. H. Sargent, *Adv. Mater.* **2011**, *23*, 3134–3138.
[22] I. J. Kramer, D. Zhitomirsky, J. D. Bass, P. M. Rice, T. Topuria, L. Krupp, S. M. Thon, A. H. Ip, R. Debnath, H.-C. Kim, E. H. Sargent, *Adv. Mater.* **2012**, *24*, 2315–2319.
[23] I. J. Kramer, L. Levina, R. Debnath, D. Zhitomirsky, E. H. Sargent, *Nano Lett.* **2011**, *11*, 3701–3706.
[24] D. Zhitomirsky, I. J. Kramer, A. J. Labelle, A. Fischer, R. Debnath, J. Pan, O. M. Bakr, E. H. Sargent, *Nano Lett.* **2012**, *12*, 1007–1012.
[25] Z. Ning, Y. Ren, S. Hoogland, O. Voznyy, L. Levina, P. Stadler, X. Lan, D. Zhitomirsky, E. H. Sargent, *Adv. Mater.* **2012**, *24*, 6295–6299.
[26] M. Burgelman, P. Nollet, S. Degrave, *Thin Solid Films* **2000**, *361–362*, 527–532.
[27] M. Burgelman, J. Verschraegen, S. Degrave, P. Nollet, *Prog. Photovoltaics: Res. Appl.* **2004**, *12*, 143–153.
[28] I. J. Kramer, E. H. Sargent, *ACS Nano* **2011**, *5*, 8506–8514.
[29] A. Goetzberger, C. Hebling, H.-W. Schock, *Mater. Sci. Eng.: R: Reports* **2003**, *40*, 1–46.
[30] J. H. Engel, Y. Surendranath, A. P. Alivisatos, *J. Am. Chem. Soc.* **2012**, *134*, 13200–13203.
[31] F. Recart, A. Cuevas, *IEEE Trans. Electron. Dev.* **2006**, *53*, 442–448.

© 2013 WILEY-VCH Verlag GmbH & Co. KGaA, Weinheim